═Light Metals═══════════════════════════════From *Light Metals 2002*, Wolfgang A. Schneider, Editor═

MODELLING THE METALLURGICAL REACTIONS DURING HOMOGENISATION OF AN AA3103 ALLOY

Arild Håkonsen[1], Dag Mortensen[2], Steinar Benum[1], Tanja Pettersen[1], Trond Furu[1]

[1]Hydro Aluminium R&D Materials Technology, N-6600 Sunndalsøra, Norway
[2]Institute for Energy Technology, N-2027 Kjeller, Norway

Abstract

The as cast microstructure of a DC cast AA3103 alloy consists of equiaxed grains with a cellular structure. The periphery of the cells contains high volume fractions of intermetallic phases and there are large variations in the solid solution level across the cells. During a typical homogenisation heat treatment the material is heated at 50 to100°C/hour up to a temperature of 500-600°C and held there for some hours. The material is then cooled to room temperature (extrusion ingot) or fed into the hot-rolling mill (sheet ingot). A model for the metallurgical reactions occurring in this system is constructed based on a cylindrical cell geometry. The as cast microstructure is adopted from a solidification model (Alstruc) that predicts the micro segregation, the volume fraction and the composition of the primary phases. A thermodynamic description of the two phases $Al_6(Mn,Fe)$ and $Al_{15}(Mn,Fe)_3Si$ is proposed, assuming matrix to be a dilute solution and the phases to be regular solutions. Fe and Mn are allowed to substitute each other completely. Precipitation, growth and coarsening of the phases are modelled individually in each position across the cell, each particle is designated to a size class and infinite diffusion is assumed inside particles. Diffusion across the cell is accounted for. Model results are compared with measured number density and size distribution of precipitates and electrical conductivity.

Introduction

Aluminium alloys with manganese as the main alloying elements (3xxx-alloys) have a wide spread application. These alloys are recognised to be highly cost effective and combine good corrosion properties and formability with moderate strength. During solidification Fe-rich particles form and most of the Mn will be in solid solution.

During the subsequent heat treatment (homogenisation, pre-heating or soaking) Mn diffuses into the Fe-rich particles formed during solidification, Mn-bearing precipitates form, and the micro segregation levels out. All these metallurgical processes strongly influence the properties during the downstream thermo-mechanical treatment of the material.

This work focuses on the metallurgical reactions that occur during the post-solidification heat treatment of an AA3103 alloy. Two types of intermetallic particles are found in this alloy, $Al_6(Mn,Fe)$ and α-$Al_{15}(Mn,Fe)_3Si$, see e.g. [28]. Both these phases have a non-stoichiometric nature where Fe and Mn can substitute each other almost completely. The dominating phase as-cast is the $Al_6(Mn,Fe)$. During heating to holding temperature Mn-bearing precipitates form. During holding the precipitates will coarsen and typically some of the $Al_6(Mn,Fe)$ (formed during solidification) will be transformed into $Al_{15}(Mn,Fe)_3Si$. In this work precipitation, growth and coarsening of non-stoichiometric phases are treated simultaneously in a domain where the solute elements and primary precipitates are distributed in space.

The precipitation kinetics in Al-Mn alloys have been investigated by several authors [1,2,3,4,5,6]. However, very few quantitative data for the size and number density of secondary precipitates are published. Many authors have previously modelled nucleation, growth and coarsening of stoichiometric phases using an average particle size (one size "class"), see *eg.* [7,8,9,10,11]. To have a more physical model which handles nucleation, growth and coarsening simultaneously, size classes of secondary precipitates have recently been introduced [12,13,14]. In these works the size classes are generated during nucleation, and the particles in each class varies in size during the calculation.

The present work is based on the recent work by Myhr and Grong [15] where the size classes are fixed (in size). The particles are put into the size class corresponding to the critical radius at the time (and position in the DAS) and the particles grow and dissolve into different size classes during the calculation. In the present work this concept is extended to handle non-constant size class widths and thus obtained a substantial reduction in the CPU time.

Model description

Main assumptions and modelling strategy

The domain of the model is a 2D section of a cylinder representing a cell, or secondary dendrite arm formed during solidification. The centre of the cylinder represents the material first to solidify, see Figure 1. The solidification model Alstruc [16] was used to predict the as-cast micro-segregation and volume fraction of the primary constituents versus solid fraction.
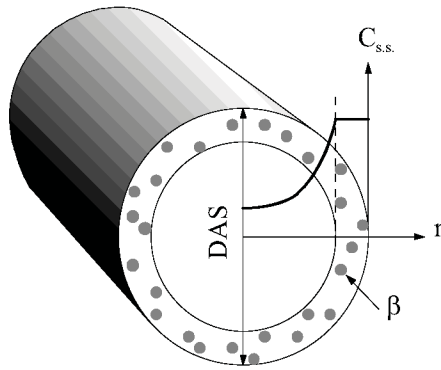

Figure 1. The domain of the model presented in this work. C_{ss} is the matrix solid solution concentration of an element and β is a phase formed during solidification.

The main assumptions in the model are:
1. In the thermodynamic description the matrix is assumed to be an *ideal solution* and the intermetallic particles are assumed to be *regular solutions*.
2. The intermetallic particles are assumed to be semi-stoichiometric.
3. All particles are assumed to be spheres.
4. The diffusion inside the particles is assumed to be infinitely high.
5. The "invariant size" and "steady state diffusion field" approximations are used in the growth law.
6. A weak coupling is applied between the growth of each particle and the "macro" diffusion in the domain.

Thermodynamic description

The phases in this work are assumed to be semi-stoichiometric in the sense that the phase is a mixture of two stoichiometric phases. More specific; the composition of the phases is given but Fe and Mn can substitute each other completely.

If we assume the matrix to be a dilute solution the activation coefficient for the elements in solution equals unity and the Gibbs energy of the matrix is given by (1) [17]. The assumption of a regular solution for the intermetallic phases implies no excess entropy ($\Delta S^{XS}=0$) and the Gibbs energy is given by (2) [17].

$$G_{matrix} = \sum_i x_i^\alpha \left(H_i - T \cdot S_i \right) + R_g T \sum_i x_i^\alpha \ln x_i^\alpha \quad (1)$$

$$G_{phase} = \sum_i x_i^\beta \left(H_i - T \cdot S_i \right) + \Delta H^{XS} + R_g T \sum_i x_i^\beta \ln x_i^\beta \quad (2)$$

Where x_i^α, H_i and S_i is mole fraction, enthalpy and entropy of element i in solid solution respectively. x_i^β is the mole fraction of element i in the intermetallic phase and ΔH^{XS} is the enthalpy of mixing. This mole fraction is in this work given by the formula of the phase and the site fraction of Fe and Mn. R_g is the gas constant and T is the temperature. For a semi-stoichiometric phase where Fe and Mn can substitute each other completely (2) becomes [18]:

$$G_{phase} = f_{Fe} G_{Fe} + f_{Mn} G_{Mn} + \Omega f_{Fe} f_{Mn}$$
$$+ R_g T \left(x_{Fe}^\beta + x_{Mn}^\beta \right) \left(f_{Fe} \ln f_{Fe} + f_{Mn} \ln f_{Mn} \right) \quad (3)$$

Where f_{Fe} is the site fraction Fe ($f_{Fe} + f_{Mn} = 1$), G_{Fe} is the Gibbs energy for the phase without Mn and Ω is an empirical constant to scale the enthalpy of mixing (here assumed to be symmetrical and temperature independent). By combining (1) and (3) we get the equilibrium solubility product of the phase:

$$K = \prod_i \left(C_{i,eq.}^\alpha \right)^{m \cdot x_i^\beta}$$
$$= K_{Fe}^{f_{Fe}} K_{Mn}^{f_{Mn}} \left(f_{Fe}^{f_{Fe}} f_{Mn}^{f_{Mn}} \right)^{m\left(x_{Fe} + x_{Mn} \right)} \exp\left[\frac{m \Omega f_{Fe} f_{Mn}}{R_g T} \right] \quad (4)$$

Where m is the number of atoms in the "molecule", $C_{i,eq.}^\alpha$ is the equilibrium solid solution concentration of element i in matrix (in wt%), x_i^β is the atomic fraction of element i in the phase, 1, 2 and 3 refer to the different alloying elements in the phase and K_{Fe} and K_{Mn} are given by:

$$K_{Fe} = A_{Fe} \exp\left[-\frac{B_{Mn}}{T} \right] \quad ; \quad K_{Mn} = A_{Mn} \exp\left[-\frac{B_{Mn}}{T} \right] \quad (5)$$

The solubility product versus composition and temperature of the phase is therefore given by 5 parameters for each phase; A_{Fe}, B_{Fe}, A_{Mn}, B_{Mn} and Ω, which all should be determined experimentally. The values of these parameters used in this work are shown in Table I.

Table I. The thermodynamic parameters for the two phases $Al_6(Mn,Fe)$ and $Al_{15}(Mn,Fe)_3Si$ used in this work.

Parameter	$Al_6(Mn,Fe)$	$Al_{15}(Mn,Fe)_3Si$.
A_{Fe}	2.2E+3 [wt%]	1.5E+12 [wt%^{4}]
B_{Fe}	9.2E+3 [K]	3.5E+4 [K]
A_{Mn}	1.35E+4 [wt%]	7E+20 [wt%^{4}]
B_{Mn}	8.5E+3 [K]	4.5E+4 [K]
Ω	0 [J/mol]	0 [J/mol]
m	7	19
V_m	9.9E-6 [m^3/mol]	9E-6 [m^3/mol]
M_i	0.034 [kg/mol]	0.031 [kg/mol]
γ	0.1 [J/m²]	0.07 [J/m²]

The chemical driving force for precipitation of one mole atoms of the phase is given by:

Table II. The molar weight, diffusion, conductivity and hardening constants of the elements used in this work.

Element	M_i [kg/mol] [19]	D_0^i [m²/s] [20]	Q^i [J/mol] [21]	k_i [µΩm] [22]	c_i [MPa/wt%$^{2/3}$] [23]
Al	0.027	-----	-----	0.026[□]	-----
Si	0.0281	2.02E-4	136,000	0.0068	9.2
Fe	0.0559	5.3E-3	183,400	0.032	-----
Mn	0.0549	3.17E-2	217,000	0.033	30.3

$$D_i = D_0^i \exp\left[-\frac{Q^i}{R_g T}\right]$$

[□] Altenpohl gives 0.0267 for this value.

$$\Delta G_m = R_g T \ln\left[\frac{\prod_i \left(C_i^\alpha\right)^{m \cdot x_i^\beta}}{K}\right] \quad (6)$$

If the composition of the phase and the matrix concentration (at the phase/matrix interface) of the other elements present in the phase are given (other elements than Al) it is now possible to derive the equilibrium concentration of Fe and Mn:

$$\frac{C_{Mn}^*}{[Mn]_{eq}^{f_{Mn}=1}} = f_{Mn} \exp\left[\frac{\Omega(1-f_{Mn})^2}{R_g T\left(x_{Fe}^\beta + x_{Mn}^\beta\right)}\right]$$

$$\frac{C_{Fe}^*}{[Fe]_{eq}^{f_{Fe}=1}} = f_{Fe} \exp\left[\frac{\Omega(1-f_{Fe})^2}{R_g T\left(x_{Fe}^\beta + x_{Mn}^\beta\right)}\right] \quad (7)$$

$[Mn]_{eq}^{f_{Mn}=1}$ is the equilibrium Mn concentration with no Fe in the system given by (4) and (5). In this work Ω is assumed to be zero (no enthalpy of mixing). This makes the exponential term in (4) and (7) equal to one.

Nucleation, growth and coarsening
The nucleation, growth and coarsening of the secondary precipitates are treated simultaneously in this work by introducing size classes of the precipitating phase [15,24]. When the phase is nucleated it is put into the size class that equals the critical size of the nuclei. The particle then moves between the size classes as it grows/dissolves. The modelling methodology for the size classes is described below.

Only the $Al_{15}(Mn,Fe)_3Si$ phase is assumed to nucleate during the homogenisation cycle. The nucleation frequency is calculated using the following nucleation law [25]:

$$\dot{N} = C_N \exp\left[-\frac{\Delta G_{hom}^* C_\theta}{k_B T}\right] \exp\left[-\frac{U_{nuc}}{R_g T}\right] \quad (8)$$

C_N, C_θ and U_{nuc} are the nucleation law parameters. C_N is proportional to the concentration of the precipitation elements in the matrix but is assumed to be a constant in this work. The effect of an incubation time in the nucleation is neglected. The following values are chosen in this work; C_N=2.2E25 [m^{-3}s^{-1}], C_θ=7.3E-2 and U_{nuc}=125000J/mole. ΔG_{hom}^* is given by :

$$\Delta G_{hom}^* = \frac{16\pi\gamma^3}{3(\Delta G_m / V_m)^2} \quad (9)$$

γ is the surface energy of the phase-matrix interface, and V_m is the volume of one mole atoms of the phase, see Table I. Misfit and strain energies are neglected.

There is an analytical solution of the growth velocity of a spherical particle of stoichiometric composition [26]. For non-stoichiometric particles it is necessary to account for the change in composition of the phase. If we assume infinite diffusion inside the particles we get the following equation for the growth velocity of a spherical particle:

$$\frac{dR_P}{dt} = \frac{C_i - C_i^*}{C_{Pi}^N - C_i^*} \frac{D_i}{R_P} - \frac{R_P}{3\left(C_{Pi}^N - C_i^*\right)} \frac{dC_{Pi}^N}{dt} \quad (10)$$

R_P is the particle radius, C_i is the average matrix concentration of element i in the actual DAS-position, C_i^* is the matrix composition of element i at the interface between the particle and matrix, D_i is the diffusion coefficient of element i in the matrix (see Table II) and C_{Pi}^N is the "normalised" particle concentration of element i accounting for differences in density of the phase and matrix. C_{Pi}^N is given by the following expression:

$$C_{Pi}^N = x_i^\beta \left(\frac{100\% M_i V_m^\alpha}{M_\alpha V_m}\right) \quad (11)$$

M_i is the mole-weight of element i, V_m^α is the molar volume of Al (1E-5 [m3/mol] is used in this work) and M_α is the molar weight of Al. The molar weight and diffusivity of the elements are given in Table II. Since the particles are assumed to be semi-stoichiometric the increase in the Fe and Mn concentrations in the particles have to be equal but with opposite signs. This together with (10) gives the following expression for the change in particle concentration of Fe and Mn:

$$\frac{dC_{PMn}^N}{dt} = \frac{1}{R_P^2} \cdot \frac{\dfrac{C_{Mn} - C_{Mn}^*}{C_{PMn}^N - C_{Mn}^*} D_{Mn} - \dfrac{C_{Fe} - C_{Fe}^*}{C_{PFe}^N - C_{Fe}^*} D_{Fe}}{\dfrac{1}{3\left(C_{PMn}^N - C_{Mn}^*\right)} + \dfrac{1}{3\left(C_{PFe}^N - C_{Fe}^*\right)}} \quad (12)$$

At the interface of the particle the surface energy will balance the chemical driving force for precipitation (6) (thermodynamic

equilibrium is assumed and strain energy neglected). The solubility product at the surface, K^*, will then be:

$$K^* = K \exp\left[\frac{mV_m 2\gamma}{R_g TR_P}\right] \tag{13}$$

If the particle is stoichiometric with only one alloying element (13) is equal to the standard Gibbs-Thomson equation [25].

The treatment of the size classes and mass balance
The diffusion equation is solved in one dimension by a finite element method along the radial direction from centre to the surface of the secondary dendrite arm:

$$\frac{\partial C_i}{\partial t} = \frac{1}{r}\frac{\partial}{\partial r}\left(rD_i \frac{\partial C_i}{\partial r}\right) \tag{14}$$

where r is the radius of the dendrite arm. The distributions of the matrix concentrations at zero time are the as cast distributions from Alstruc. The same spatial discrete resolution as in Alstruc is applied (75 elements biased against the surface of the dendrite). In the time integration the time step is adjusted by a maximum absolute change of matrix concentration for all alloying elements at a radial position during one time step (0.00005wt% in the calculations shown here). The observed change of matrix concentration stems from both micro-segregation and growth of particles during the time step.

In the beginning of a new time step precipitation, growth and coarsening of all type of particles are calculated in all the radial positions. The content of the alloying elements are summed up afterwards, and the differences are added or removed from the matrix concentrations before the microsegregation is calculated again. The sum of the matrix concentration and the amount of an element bound into the particles are kept track of in each radial position, and is given by:

$$C_i^{Bal} = C_i + 100wt\% \cdot \frac{M_i}{\rho_{tot}} \cdot \sum_\beta \frac{x_i^\beta f^\beta}{V_m^\beta} \tag{15}$$

Where ρ_{tot} is the total density (2700kg/m^3 in this work), f^β is the volume fraction of particle type β, and V_m^β is the volume of one mole of phase β. The mass balance is expressed as the integral in space of C^{Bal}_i over the dendrite arm and it equals the total or the nominal content of the alloy element number i in the alloy.

$$C_i^0 = \frac{8}{DAS^2} \int_0^{DAS/2} rC_i^{Bal} dr \tag{16}$$

Where DAS/2 is the radius of the dendrite arm.

The particles are distributed in a range of size classes for each radial position in the dendrite. This work is based on the work of Myrh and Grong [15] but is extended to handle non-constant size widths. Each class numbered as k corresponds to a selection of particles with radii between r_k and r_{k+1}. The number of particles per cubic meter inside the class is denoted n_k. Then, instead of calculating the growth velocity of the mean size of the particles,

the growth (or dissolution/coarsening) velocity V_k is calculated for each radii r_k.
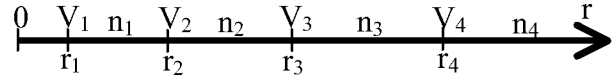
Figure 2. Illustration of particle size classes. The size of each class may be biased such that small intervals are applied for small radii.

The particles are moved between the classes based on the calculated velocities. In solving this problem we can take advantage of the fact that all velocities are negative below the critical size of the nuclei, and all velocities are positive above. An upwind solution is found by first searching for the class which includes the critical radii, and then by solving the transport of particles in both direction from this point. E.g. if the critical radii is located in class number 1, then V_2 and V_3 are positive, and the new number density of particles in class number 2 is calculated by:

$$\Delta n_2 = n_1 \frac{V_2 \Delta t}{r_2 - r_1} - \left(n_2 + n_1 \frac{V_2 \Delta t}{r_2 - r_1}\right)\frac{V_3 \Delta t}{r_3 - r_2} \tag{17}$$

Only the available number of particles is moved. In the calculations shown here r_1 is equal to $5 \cdot 10^{-10}$m for the secondary particles, r_2 is $1 \cdot 10^{-9}$m and the next values are calculated by increasing the values according to the following relation:

$$r_{k+1} = r_k + 1.09 \cdot (r_k - r_{k-1}) \tag{18}$$

A number of 50 classes for the secondary precipitates is applied. For the primary precipitates only one size class is used. This class is not fixed in size but follows the particles as they grow and dissolve. The initial radius of the primary precipitates is set to 4µm in this work.

The fraction of Mn in the non-stoichiometric particles will not be equal in the different size classes since the particles do not have a common history. After calculating the new number densities the new Mn fraction is calculated by a number average between "old" and "new" particles of the same size.

Calculation of hardness and electrical conductivity
A general expression for the flow stress in a material is

$$\sigma = \sigma_0 + \sigma_{ss} + \sigma_p + f(\rho, \delta) \tag{19}$$

where σ_0 is the friction stress, σ_{ss} is the contribution to the flow stress from atoms in solid solution, σ_p is the contribution from particles and $f(\sigma, \delta)$ is the contribution from the dislocations. An approximate expression for the contribution due to particles is [26]:

$$\sigma_p = c_p \frac{Gb}{\lambda} \ln\left(\frac{\overline{R}_P}{b}\right) \tag{20}$$

where c_p is a constant, G is the shear modulus, b is the Burgers vector, λ is the inter particle distance and $\overline{R}_P$ is the average

radius of the phase. Similarly, the contribution from the atoms in solid solution can approximately be given by [24]:

$$\sigma_{ss} = \sum_i c_i \left(C_i^{ss} \right)^{2/3} \tag{21}$$

where c_i is a constant for element i and C_i^{ss} is the average solid solution concentration of element i in the matrix.

During solidification dislocations will form as a result of the uneven cooling rates in the different positions in the billet. Hence, during the post solidification heat treatment, recovery reactions will occur according to the following equation [27]:

$$\frac{d\rho_i}{dt} = -B^\rho v_D b \rho_i^{3/2} \exp\left[-\frac{Q_\rho}{R_g T} \right] 2 \sinh\left[\frac{A_\rho G b^4 \rho_i^{1/2}}{k_B T} \right] \tag{22}$$

The definition and values used in the equation can be found in Table III. The flow stress is hence given by:

$$\sigma = \sigma_0 + \sum_i c_i \left(C_i^{ss} \right)^{2/3} + c_p \frac{Gb}{\lambda} \ln\left(\frac{\overline{R}_p}{b} \right) + \alpha_1 M G b \sqrt{\rho_i} \tag{23}$$

Table III. Definition and values of the parameters used in the calculation of yield stress.

Parameter	Definition	Value
c_P	Particle hardening constant	0.29
G	Shear modulus of Al	2.55e+4 MPa
b	Burgers vector of Al	2.86E-10 m
λ	Average Interparticle distance	$\lambda = N^{-1/3}$
$\overline{R}_P$	Average particle radius	Number average
α_1	Internal dislocation hardening constant	0.3
M	Taylor factor	3
ρ_i	Internal dislocation density	Calculated from ρ_i^0
ρ_i^0	Initial value of ρ_i	1.8E+13 m^{-2}
A_ρ	(Average distance between atoms in solid solution)/b	$A_\rho = \frac{1}{2} x_{Mn}^{ss}{}^{-2/3}$
B^ρ	Constant in the recovery eq.	2E+6
v_D	Debye frequency	1E+13
Q_ρ	Activation energy for solute diffusion	210,000 J/mol

To obtain the hardness from the calculated flow stress values the following empirical equation was used [24]:

$$HV = 0.33\sigma + 16 \tag{24}$$

The electrical conductivity, κ, of an alloy is normally predicted using equation (25) [23]. Where k_{Al} is the electrical resistivity of pure aluminium, k_i is a constant for element i and C_i^{ss} is the average solid solution concentration of element i in the matrix. The k-values are given in Table II.

$$\frac{1}{\kappa} = k_{Al} + \sum_i k_i C_i^{ss} \tag{25}$$

Experiments

This work is concentrated on only one alloy, AA3103. The chemical composition of the alloy is given in Table IV. The material was cut from the mid radius of a 178mm diameter extrusion billet.

Table IV. The chemical composition of the investigated AA3103 alloy.

Element	Fe	Si	Mn	Others
[Wt%]	0.54	0.12	1.06	<0.02

Four homogenisation treatments were applied to the material (started at room temperature):

A: 100K/h heating to 550°C → Holding at 550°C for 24h
B: 100K/h heating to 570°C → Holding at 570°C for 24h
C: 100K/h heating to 590°C → Holding at 590°C for 24h
D: 100K/h heating to 610°C → Holding at 610°C for 24h

During heating and holding samples were quenched and the precipitate size distribution and precipitate number density were measured in TEM. In addition, hardness and electrical conductivity were measured. The measurements are shown together with the model predictions below.

Results

Figure 3 shows how the secondary precipitates appeared in TEM during heating, quenched from 550 and 610°C. The density of particles is higher and the particle size is smaller in the 550°C sample compared to the 610°C sample. Most of the precipitates are plates but some rods can also be seen. The measured and calculated hardness during heating and holding at 550, 570, 590 and 610°C are shown in Figure 4. A general good agreement can be seen except from the calculated peak during heating at around 17000s, corresponding to around 500°C. The calculated hardness during holding at 550°C is generally somewhat high. Figure 5 is a comparison between the measured and calculated electrical conductivity during heating and holding at different temperatures. The conductivity was largely overestimated during heating at around 18000s, corresponding to 500-550°C. During holding the model predicts higher conductivity for the low temperatures. The agreement is however good for the highest temperature. The measured and calculated cumulative size distributions are shown in Figure 6. The measurements show a wider spread in the sizes compared to the calculations.

The measured and calculated number densities of the secondary precipitates are shown in Figure 7. A general good agreement can be seen. This means that both the nucleation and coarsening are well reproduced in the model. The growth was however overestimated (too large increase in the conductivity during holding).

The calculated volume fraction of the phases and the site fraction Mn in the phases during heating and holding at 610°C are shown in Figure 8 and 9 respectively. Only small changes in the volume fraction of the primary phases were predicted. The calculated site
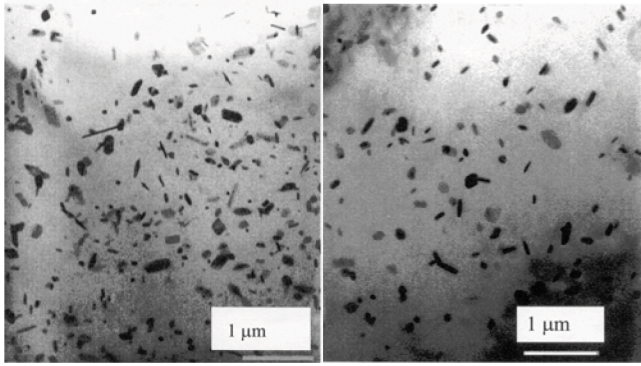
Figure 3. Pictures of the secondary precipitates (TEM) during heating (and quenching) from 550°C (left) and 610°C (right).

fraction Mn in the secondary precipitates was first decreasing during heating and thereafter increasing to 0.95.

During holding f_{Mn} decreased for the secondary precipitates and increased in the primary precipitates approaching 0.56 for $Al_6(Mn,Fe)$ and 0.48 for $Al_{15}(Mn,Fe)_3Si$ after 24hours at 610°C.

Figure 10 is a 3D plot of the solid solution level of Si versus DAS-position and time (heating and holding at 610°C). At the start of heat treatment there is a strong micro-segregation of Si over the DAS. During heating (before the nucleation of secondary precipitates starts) this segregation is levelling out. After this the Si content is decreasing due to precipitation and growth of the $Al_{15}(Mn,Fe)_3Si$ phase. When the precipitates dissolve again (still during heating) the Si content increases. Finally, during holding the Si content decreases again due to an increase in the volume fraction $Al_{15}(Mn,Fe)_3Si$.
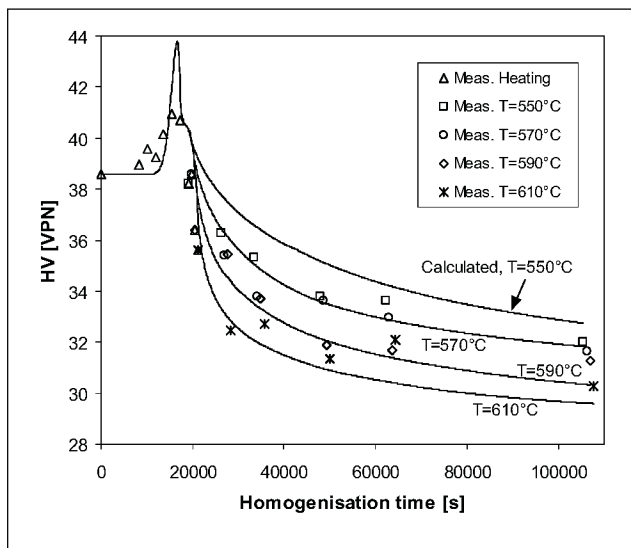
Figure 4. Measured and calculated hardness during heating (100K/h) and holding at 550, 570, 590 and 610°C.
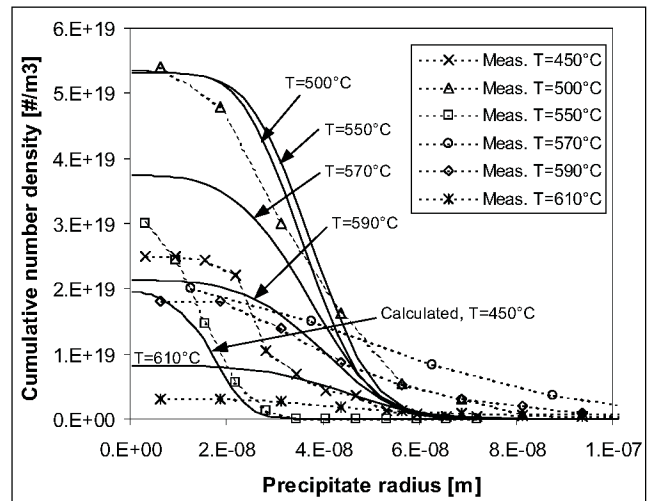
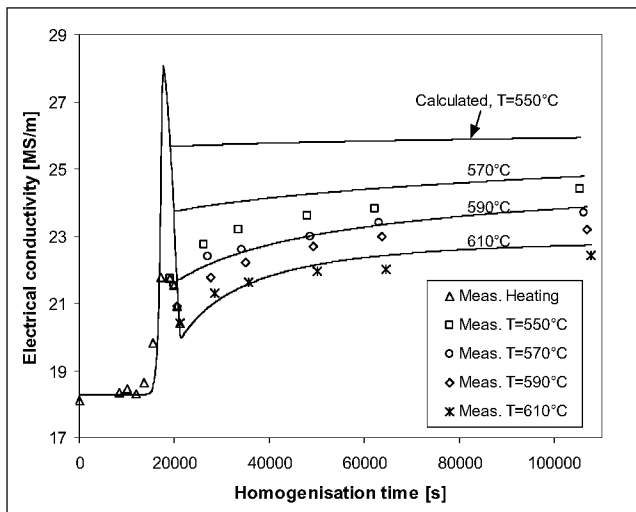Figure 6. Measured and calculated cumulative size distribution of dispersoids during heating.

Figure 5. Measured and calculated electrical conductivity during heating (100K/h) and holding at 550, 570, 590 and 610°C.
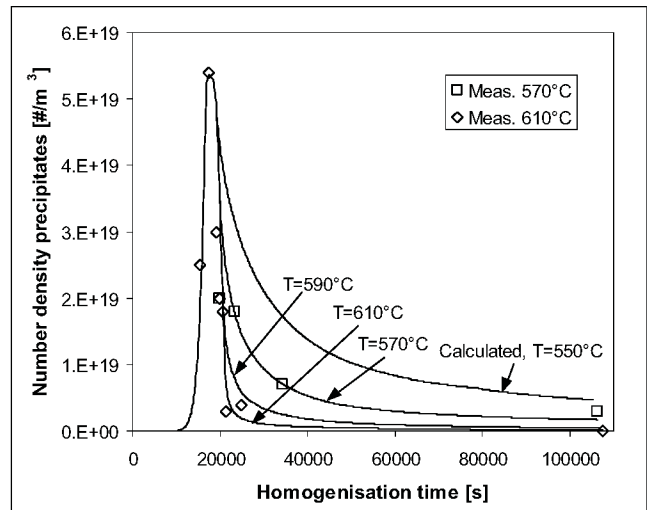

Figure 7. Measured and calculated number density of dispersoids during heating and holding.
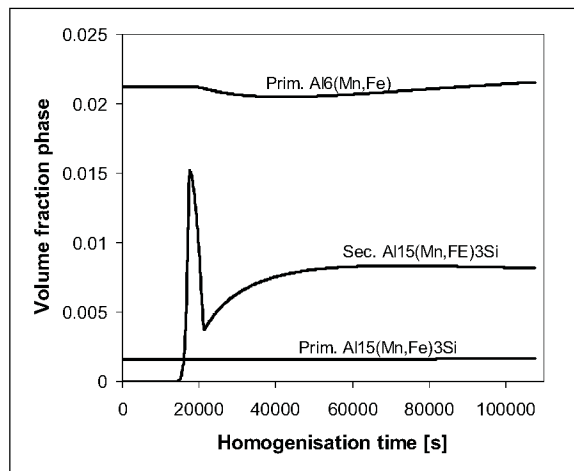
Figure 8. Calculated development of the volume fraction of the different phases during heating (100K/h) and holding at 610°C.
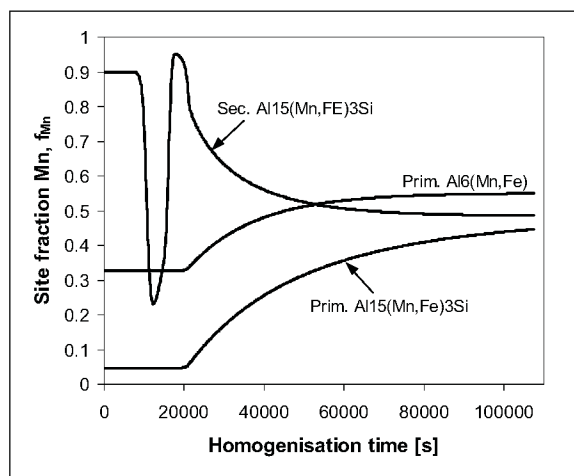

Figure 9. Calculated development of the site fraction Mn in the phases during heating (100K/h) and holding at 610°C.
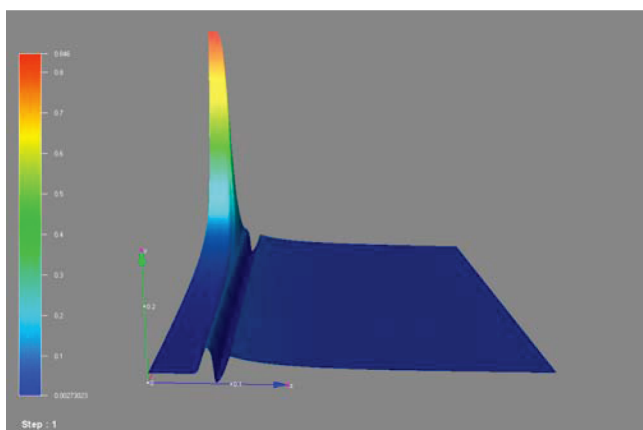

Figure 10. Calculated distribution of the solid solution level of Si versus DAS-position (axis pointing inwards) and time (axis pointing to the right).

Discussion

The thermodynamic model used in this work (equations (4)-(7)) is the simplest imaginable to describe non-stoichiometric phases. The constants in Table I are based on our available experimental data for these phases. The model predictions will be sensible to the thermodynamic description but the observed disagreement between measurements and calculations in this work is probably not due to errors in the thermodynamic description.

The nucleation model (equation (8)) is the classical way of model nucleation. The equation does often have an incubation time term. This term was originally introduced to explain an observed delay in nucleation in isothermal studies. In this work a slow heating rate was used and the need of an incubation time is not believed to be necessary (equilibrium distribution of clusters during heating). The parameters in the nucleation law were tuned to give good correlation with measured number densities and will not be discussed further.

The growth shortly after nucleation seems to be overestimated in the model, see Figure 5. The number densities are of the correct order but the conductivity is too high. Several possible explanations could be the reason for the differences between the measured and modelled volume fraction during early growth. We assume sphere particles while the morphology of the particles is more plate-like. The basic assumption of a stationary diffusion field around the particles can also be questioned. In the model the composition of the secondary precipitates change very rapidly during heating. It is difficult to imagine that the diffusion field has sufficient time to become "stationary" during these rapid changes. If there are significant strain energies or mismatch energies related to the growth of the precipitates this will slow down the growth. To obtain good correlation temperature, or size, dependent energies have to be introduced to reproduce the volume fraction precipitates for higher temperatures. Normally these energies are considered to be a volume constant for the phase. The precipitates were observed to be unevenly distributed inside the matrix (locally inside the DAS). In the model however the particles are uniformly distributed within the DAS-element and therefore have more matrix to grow into. All these points will slow down the average growth. It is also possible that the precipitates influence the conductivity measurements.

Transformation of primary $Al_6(Mn,Fe)$ to $Al_{15}(Mn,Fe)_3Si$ is known to occur in Al-Mn-Fe-Si alloys [28, 29]. Very little transformation is expected in the alloy investigated in this work. This is due to the high Fe and low Si content [28].

Acknowledgement

References

[1] H. Hirasawa, "Precipitation process of Al-Mn and Al-Cr supersaturated solid solution in presence of age hardening phases", Scripta Met. Vol. 9, 1975, pp. 955-958.

[2] G. Vörös and I. Kovacs, "Precipitation processes in DC-cast AlMn(Fe,Si) alloys", Key Engineering Materials Vols. 44 & 45, 1990, pp. 247-256.

[3] I. Moricz et al., "The effect of Fe and Si on the precipitation behaviour of Mn in Aluminium", Key Engineering Materials Vols. 44 & 45, 1990, pp. 265-270.

[4] R. G. Kamat, J. N. Yelim and S. Saimoto, "Morphology and precipitation of α-Al(Fe,Mn)Si phase in hot rolled AA3004", Z. Metallkd. **86**, 1995, pp. 49-53.

[5] S. Ding, J. Qiu and J. G. Morris, Aluminium alloys for packaging III, Ed. By S.K. Das, The Minerals, Metals & Materials Society, 1998, pp. 39-47.

[6] L. Lodgaard and N. Ryum, Aluminium Transactions, Vol. 2, No. 2, 2000, pp. 267-275.

[7] P. Haasen and R. Wagner, "High-resolution microscopy and early-stage precipitation kinetics", Met. Trans. A, Vol. 23A, 1992, pp. 1901-1914.

[8] T. E. Johnsen and B. R. Henriksen, "Modelling of precipitation and dissolution of Mg2Si in AlMgSi alloys", Proceed. of the 4th international conference on aluminium alloys, Vol. I, ed. T. H. Sanders Jr. and E.A. Starke Jr., 1994, pp. 612-619.

[9] O. R. Myhr et al. "Process model for welding of Al-Mg-Si exstrusions, Part 1: Precipitate stability", Science and Technology of Welding and Joining, Vol. 2, No. 6, 1997, pp. 245-253.

[10] D. Godard et al., "The modelling of the heterogeneous precipitation in Al_Zn-Mg-Cu alloys during quenching", Proceed.. Of the Int. Conf. On solid-solid phase transformations '99, Ed. By M. Koiwa, K. Otsuka andT. Miyazaki, The Japan Institute of Metals, 1999, pp. 145-147.

[11] B. Dutta, E. J. Palmiere and C. M. Sellars, "Modelling the kinetics of strain induced precipitation in Nb Microalloyed steels", Acta Mater. Vol. 49, 2001, pp. 785-794.

[12] A. Deschamps and Y. Brechet, "Influence of predeformation and ageing of an Al-Zn-Mg alloy-II. Modeling of precipitation kinetics and yield stress", Acta Mater. Vol. 47, 1999, pp. 293-305.

[13] C. Sigli, "Nucleation, growth and coarsening of spherical precipitates in aluminium alloys", Materials Science Forum Vols. 331-337, 2000, pp. 513-518.

[14] J. D. Robson and P. B. Prangnell, "Dispersoid precipitation and process modelling in Zirconium containing commercial aluminium alloys", Acta Mater. Vol. 49, 2001, pp. 599-613.

[15] O. R. Myhr and Ø. Grong, "Modelling of non-isothermal transformations in alloys containing a particle distribution", Acta mater., Vol. 48, 2000, pp. 1605-1615.

[16] A. L. Dons et al., "The Alstruc microstructure solidification model for industrial aluminium alloys", Met. Trans. *A*, Vol. 30A, 1999, pp. 2135-2146.

[17] P. Gordon, "Principles of phase diagrams in materials systems". Krieger Publishing Company, Malabar, Florida, 1968.

[18] C. Sigli, L. Maenner, C. Sztur and R. Shahani, "Phase diagram, Solidification and heat treatment of aluminium alloys", Proceedings of ICAA-6, 1998, pp. 87-98.

[19] Aylward & Findlay, Si Chemical Data, Sec. Ed. Jacaranda Wiley Ltd., 1974.

[20] H. Bakker. Diffusion in solid metals and alloys, Vol. 26, Landort-Börnstein, Springer-Verlag, Berlin, 1990.

[21] D. Altenpohl, Aluminium und aluminiumleigierungen, Sprenger Verlag, 1965.

[22] ASM Handbook, Vol. 2. Properties and selection: Nonferrous alloys and special-purpose materials, ASM International, 1990.

[23] O. R. Myhr, Ø. Grong and J. Andersen, "Modelling of the age hardening behaviour of Al-Mg-Si alloys", Acta mater. Vol. 49, 2001, pp. 65-75.

[24] R. Wagner and R. Kampmann, Mater. Sci. Technol.-A Comprehensive Treatment, P. Haasen, ed., Weinhiem, VCH, 1990, Vol. 5, p. 213.

[25] H. B. Aaron, D. Fainstain and G.R. Kotler: J. Appl. Phys., 1970, Vol. 41, p. 4404.

[26] M. F. Ashby, "The theory of the critical shear stress and work hardening of dispersion-hardened crystals", in Proc. Second Bolton Landing Conf. On Oxide Dispersion Strengthening, Gordon and Breach, Science Publishers, Inc., New Yorc, 1968, pp. 143-205.

[27] E. Nes, "Modelling of work hardening and stress saturation in FCC metals", *Progress in materials science* Vol. 41, 1998, pp. 129-193.

[28] E. Trømborg, A. L. Dons and L. Arnberg, "Investigation of the Al6(Mn,Fe) → α-Al(Mn,Fe)Si phase transformation during homogenization of AA3003 and AA3004 aluminium alloys", Proceed. of the 3th international conference on aluminium alloys, Vol. II, ed. L. Arnberg, O. Lohne, E. Nes and N. Ryum, 1992, pp. 270-275.

[29] H. Cama et al., "Intermetallic phase selection and transformation in aluminium 3xxx alloys", Proceed. of the 4th decennial international conference of solidification processing, Sheffield, 1997, pp. 555-558.